electronics

MDPI

Article

Wireless Charging Concave Coil Design for UAVs

Langtao Yu, Li Wu *, Yuyu Zhu, Xin Cao, Guozheng Zhang and Shicheng Xiang

School of Information Engineering, Southwest University of Science and Technology, Mianyang 621010, China; swust_ylt@163.com (L.Y.); zhuyuyu@swust.edu.cn (Y.Z.); caoxin@swust.edu.cn (X.C.); zgz13625647291@163.com (G.Z.); xiangshicheng2021@163.com (S.X.)
* Correspondence: 15182303569@163.com; Tel.: +86-151-8231-3252

Abstract: This paper proposes an orthogonal concave coupling mechanism based on wireless charging for unmanned aerial vehicles (UAVs); the original edge adopts a concave transmitting coil. So as not to occupy the gimbal position at the receiving end, the receiving coil is installed on the landing gear of the UAV perpendicular to the transmitting coil to form an orthogonal coupling magnetic field. This study conducted a finite element simulation of the coupling mechanism using Ansys Maxwell to test the mechanism's coupling capability and anti-offset performance. The spatial distribution of the system's magnetic field was constrained, and the magnetic flux leakage of the system was reduced by optimizing the transmitter structure. The system employed a double-sided LCC compensation topology network and used wireless communication to achieve constant voltage/constant current closed-loop control. Finally, the experimental platform was built, and the results show that the system output power was able to reach 960 W with 85.7% efficiency, and could realize the closed-loop control of charging with 48 V constant voltage and 20 A constant current. The system has the advantages of being small in size, lightweight (290 g) and easy to install, and the receiver device has strong resistance to offset.

Keywords: drones; wireless charging; concave coupling mechanism; LCC

Citation: Yu, L.; Wu, L.; Zhu, Y.; Cao, X.; Zhang, G.; Xiang, S. Wireless Charging Concave Coil Design for UAVs. *Electronics* **2022**, *11*, 1962. https://doi.org/10.3390/electronics11131962

Academic Editors: Yun Yang and Ka Wai Eric Cheng

Received: 31 May 2022
Accepted: 21 June 2022
Published: 23 June 2022

1. Introduction

In recent years, the use of unmanned aerial vehicles (UAVs) in civilian and military fields has become increasingly widespread, but the complex application environment has also revealed the shortcomings of the current rotary-wing drones in terms of battery life. Most UAVs do not last more than 30 min, and manual charging is time consuming and laborious, affecting flight efficiency; as a result, they are only able to perform short and close-range tasks [1,2], significantly limiting the scope of UAV applications and work modes. Therefore, effectively extending the flight time of UAVs is a vital issue.

Two methods are generally adopted to extend the flight time of UAVs. One is to increase the battery capacity [3]; however, a standard UAV has a limited load capacity, and this method increases its workload. The other way is to charge the battery artificially, but this increases the cost and limits the operating range of the UAV. Richardson proposes [4] extending the flight time by adjusting the flight trajectory of the UAV to take advantage of wind energy, but the environment influences this method too much, and the flight path is restricted. P. Oettershagen et al. propose [5] adding photovoltaic cells to UAVs, but this method relies on solar radiation, limiting the UAV's flight period. Therefore, the more flexible method of using a magnetic field coupled with UAV wireless charging technology [6] has been increasingly discussed. This method is based on the law of electromagnetic induction, using a high frequency alternating coupled magnetic field between the transmitting and receiving coils to transmit electrical energy [7]. This kind of magnetically coupled resonant wireless power transmission system can achieve long-distance transmission due to the effective coupling of the transmitting and receiving coils. Therefore, the design of the coupling mechanism [8,9] is the key to the system design.

Taking into account the special body mechanism of UAVs, several approaches are proposed in the literature. Kumar et al. [10] place the receiving coil on the UAV rotor to achieve a 35 W UAV wireless charging system, and the receiving coil has the function of protecting the rotor. However, this method reduces the flexibility of the UAV and is only applicable to small UAVs which cannot perform high power transmission. Song et al. [11] achieve 200 W power transmission using a multi-layer transmitting circular coil, and the system charging efficiency is maintained at 91% when the offset is less than 20 cm, but the system has not been studied for closed-loop charging control, and when the offset occurs, the system transmission power drops sharply, affecting the stability of the system. The planar hollow coil is mounted under the control board of the frame [12], and a DC-DC circuit is added after the secondary rectifier circuit to achieve a constant current charge with a transmission power of 70 W and an efficiency of 89%, but the receiving coil of this system is located in the abdominal position of the UAV, which may lead to a large amount of magnetic flux entering the body of the UAV, which could interfere with the equipment. The three-coil coupling scheme proposed in [13,14] uses relay coils for energy transfer to improve the offset resistance of the system, but the relay coils generate a large amount of energy loss, which reduces the transmission efficiency of the system, and the coupling structure is not easy to install. In [15–17], multiple transmitting coils are used to generate a large charging area to improve the system's anti-offset characteristics, but this method requires precise capture of the UAV's landing point. Current coil localization methods rely on additional detection hardware and complex detection strategies and, in addition, should reduce the mutual inductance between adjacent coils, which increases the complexity of the system. Han et al. propose [18] an omnidirectional UAV wireless charging system using dual three-dimensional transmitting coils, which has the advantages of simple structure and low cost, but its electromagnetic compatibility performance is poor. This approach poses a more significant threat to the hardware structure of UAVs.

In order not to occupy the abdominal space of the UAV and to increase the transmission distance between the coils of the system, the multi-inverse parallel square spiral coil proposed by [19] can effectively improve the charging height by 5 cm in the case of a uniform magnetic field, and the reduced efficiency is less than 3% when the offset occurs. However, the single-coil design of this structure is too complicated, and the energy loss is relatively large. The orthogonal coupling structure proposed in [20] mounts the receiver coil on the UAV's leg without occupying the gimbal position and achieves a UAV wireless charging system with 500 W charging power that is also lightweight and has low magnetic leakage interference. However, the lateral area of this receiver coil is too large and not fully embedded in the UAV's leg, making it highly susceptible to damage when landing. Song et al. [21] improve the anti-offset capability of the system by installing three coils with ferrite at the bottom of the three landing gear legs of the UAV, but the need to change the structure of the original landing gear reduces the applicability of the device. Campi et al. [22] propose a wireless charging system with multiple coupling devices of three receiver coils and three transmitter coils with a total system power transfer efficiency of 72%. When the UAV lands on the charging platform, the receiver device is inserted into the transmitter device, which enhances the coupling capability of the system, but the circular-shaped notch is easy for foreign objects to enter, which affects the system operation and is not practical.

Some studies [23,24] have found that when the UAV lands autonomously, a precise landing cannot be achieved, and the coupling device cannot be aligned, resulting in a decrease in the transmission power and efficiency of the system. At present, the coupling structure for UAV wireless charging mainly concentrates on the performance of the planar configuration, which adopts primarily face-to-face charging. This brings the problems of poor adaptability to UAV body structure and strong magnetic leakage interference [25]. Compared with the planar structure, the three-dimensional coupling structure reduces the coupling capacity of the two coils to a certain extent. However, it improves the offset

resistance of the system, so it is easier to adapt the three-dimensional coupling structure to the UAV fuselage structure in the UAV wireless charging system.

As shown in the above studies, the coupling device determines the electric energy transfer capability of the system. Given the poor offset resistance of the UAV wireless charging system and the complicated installation conditions of the receiving coil, this paper proposes a design for a wireless charging system with good offset resistance characteristics in which the receiving coil is installed on the landing gear and orthogonal to the concave transmitting coil. The use of a small and lightweight receiving coil solves the problem that the receiving end in the UAV wireless charging system is not suitable for installation and reduces the workload of the UAV. For this study, a finite element analysis was conducted using Ansys-Maxwell, and the coupling device was found to have good magnetic field distribution and strong coupling capability. Finally, a 960 W prototype was built to verify the effectiveness of the coupling mechanism.

2. Concave Coupling Mechanism Design

2.1. Wireless Charging Coupling Mechanism for Drones

To make the receiver coil more easily adaptable to the structure of the UAV fuselage and not take up space on the gimbal and other equipment, the receiving coil is placed on the landing gear of the UAV. The overall structure diagram of the system is shown in Figure 1. The transmitting coil adopts a concave structure, which improves the anti-offset capability of the system. The proposed coupling structure is divided into a transmitting side and a receiving side, as shown in Figure 2. The transmitting side consists of two horizontal rectangular coils and a concave ferrite core, two vertical rectangular coils and ferrite on both sides, and an aluminum base plate. Ferrite is mainly used to direct the main magnetic flux, reduce the magnetic resistance of the magnetic circuit, reduce the magnetic field leakage of the system and improve the coupling capacity of the system. Aluminum plates enhance the mechanical strength of the coupling device. The receiving side consists of a rectangular coil perpendicular to the ground, which effectively receives the horizontal magnetic flux from the transmitter, and the structure can be easily embedded in the landing gear of the UAV without altering the structure of the UAV's fuselage and without increasing the resistance of the UAV during flight.

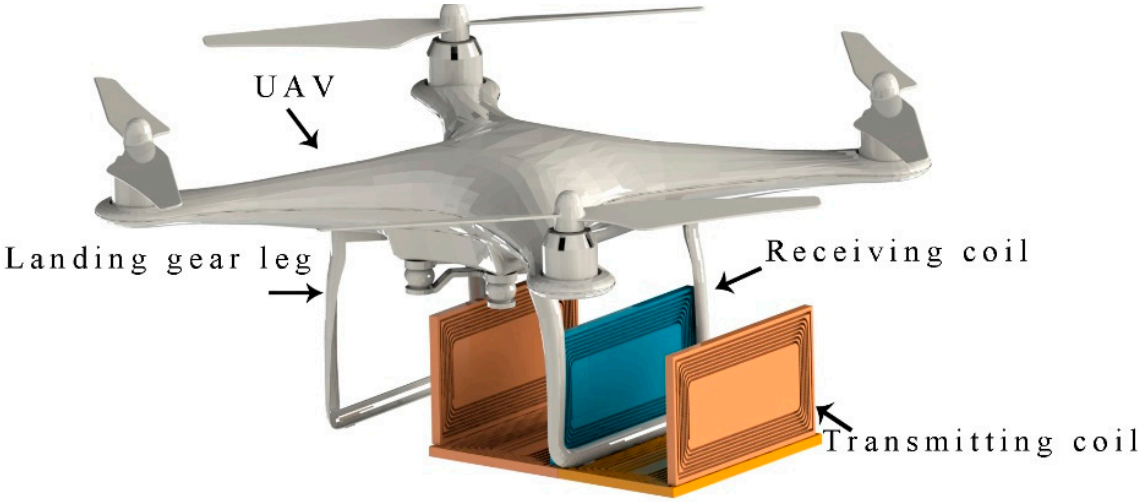

Figure 1. Diagram of a wireless charging system for drones.

The current direction in the whole coupling structure is symmetrically distributed with the receiving coil as the axis, realizing an effective coupling between the transmitting and receiving ends. The magnetic field components are shown in Figure 3, with the transmitting field distributed near the transmitting platform. The symmetrically distributed current direction also improves the system's resistance to offset to a certain extent.

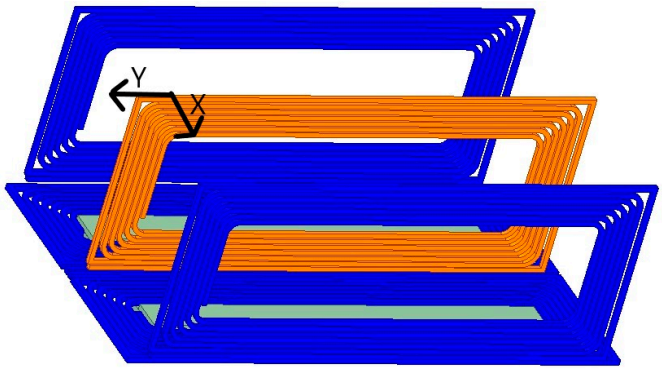

Figure 2. Concave coupling structure of the drone.

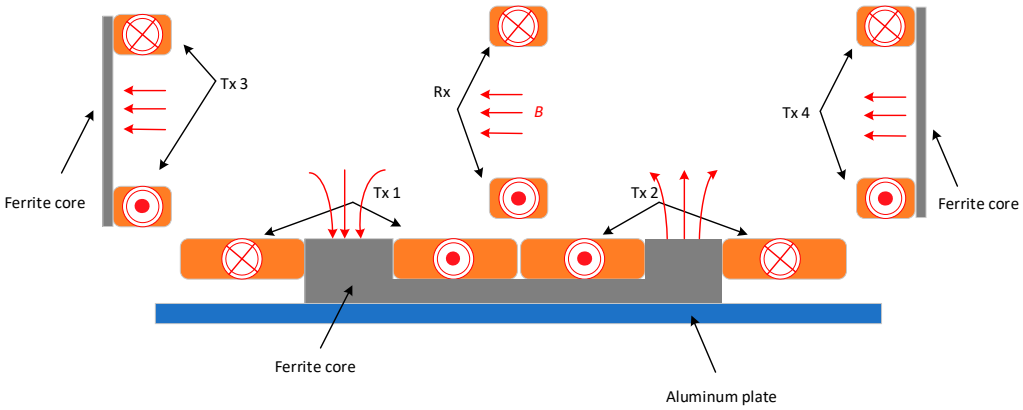

Figure 3. Magnetic field distribution of the coupled structure.

Adding a magnetic core is an effective way to improve the coupling capacity and system efficiency. Manganese zinc ferrite with saturation magnetic induction strength, B_s, high permeability, μ, and low resistivity was selected for the material. The concave ferrite cores are placed at the transmitter end instead of spreading the ferrite all over the bottom. This design approach ensures that the system has a higher coupling capacity and better resistance to offsets. This is because when the receiving coil is shifted to the leftmost or rightmost side of the transmitter end, the system mainly relies on the vertical coils on the left and right sides for energy transmission, while the horizontal coils at the bottom produce opposite magnetic fields causing partial magnetic field offset, which will reduce the coupling capacity of the system. The concave ferrite cores weaken the magnetic field to a certain extent and improve the coupling capacity of the system.

2.2. Design of Coupling Mechanism Dimensions

Figures 4 and 5 show the top and paramount views of the coupling structure, respectively. When the type of UAV is determined, the dimensions of the UAV landing gear are determined accordingly, and therefore the receiving coil length L3 and the gap H2 between the receiving and transmitting coils are also determined. As the two horizontal transmitting coils are located next to each other, the number of turns, turn spacing and Litz wire diameter of the transmitting coil are determined; W2, W3, and W4 can be represented by W1, and W5 is the diameter of the receiving coil, from which it follows that L2 can be represented by L1. Thus, the final parameters to be determined are L1, W1, H1; the number of turns, N, of the transmitting and receiving coils; the turn spacing, p; and the diameter, w, of the Leeds wire.

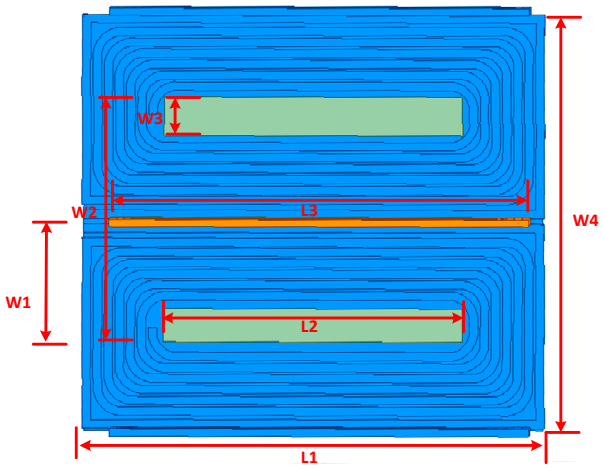

Figure 4. The top view of the coupling structure.

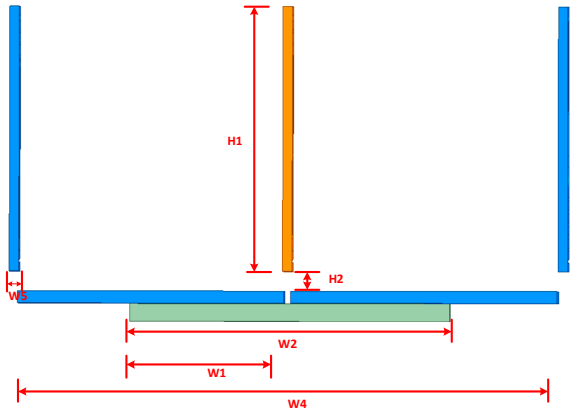

Figure 5. The paramount view of the coupling structure.

The final output current of this system is 20 A; when the system is in resonance, the current flowing through the coil will be greater than the output current. Taking into account the skin effect, the larger the diameter of the copper wire due to AC resistance caused, the greater the loss here. Take the peak current flowing through the coil, which is $\sqrt{2}$ times the output current, and choose the diameter, w, for a 3.65 mm Leeds wire winding coil. In this study, to facilitate the processing of the mold and minimize the size of the coil, the turn spacing, p, was set to 1 mm.

Assuming that the self-inductance of the transmitting and receiving coils are L_1 and L_2, and the current flowing through them is I_1 and I_2, the transferred power, P, of the coils can be easily calculated according to the equivalent model of mutual inductance of the coils as

$$P = \omega M I_1 I_2 = 2\pi f k \sqrt{L_1 L_2} I_1 I_2 \tag{1}$$

where $P = 960W$, because the receiving coil and the four transmitting coils are approximately the same sizes, so

$$L_1 \approx 4L_2 \tag{2}$$

For a single spiral structured coil, the schematic diagram is shown in Figure 6 and is obtained from Weil's formula

$$L = \frac{N^2 (D_{outer} - N(w+p))^2}{16 D_{outer} + 28N(w+p)} \times \frac{39.37}{10^6} (H) \tag{3}$$

where D_{outer} is the coil width, because the coil has not yet been designed, to leave a certain space for the UAV landing gear here takes D_{outer} = 100 mm. The (1)–(3) joint can roughly accommodate the number of turns of the transmitting and receiving coil N = 7.

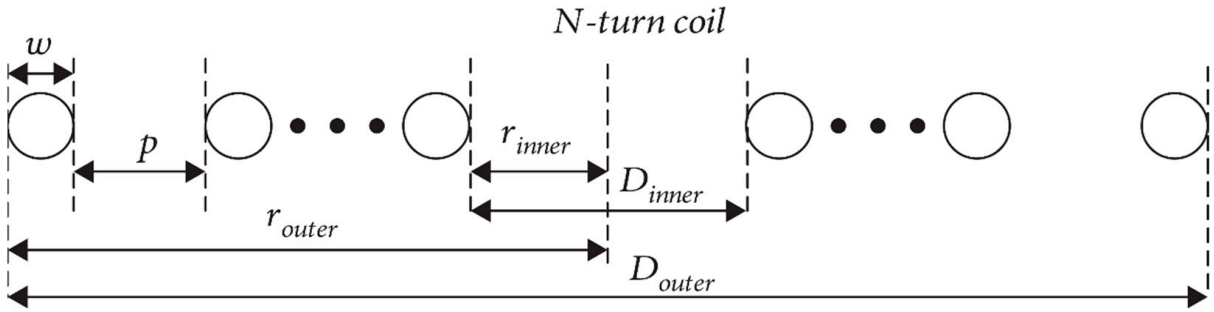

Figure 6. Schematic diagram of the spiral coil cross-section.

In order to improve the coupling performance of the system, the maximum coupling coefficient of the system was determined by finding the optimum values of L1, W2, and H1 at the alignment position through an analysis method based on ANSYS Maxwell finite element simulation.

L1 is the length of the transmitting coil, and varied in the range of 250–350 mm; the value of the coupling coefficient, k, was obtained using Maxwell simulation analysis. The simulation results are shown in Figure 7. As L1 increases, the receiving coil receives more and more horizontal magnetic flux, but the length of the UAV frame is already determined, so the length of the receiving coil L3 was 294 mm. When L1 is much larger than L3, the change in k is small. As L1 continues to increase, the leakage from the coupling device will also increase, and the coupling coefficient gradually decreases. Therefore, after analyzing the simulation results, L1 was set to 320 mm, which is when the coupling coefficient was greatest.

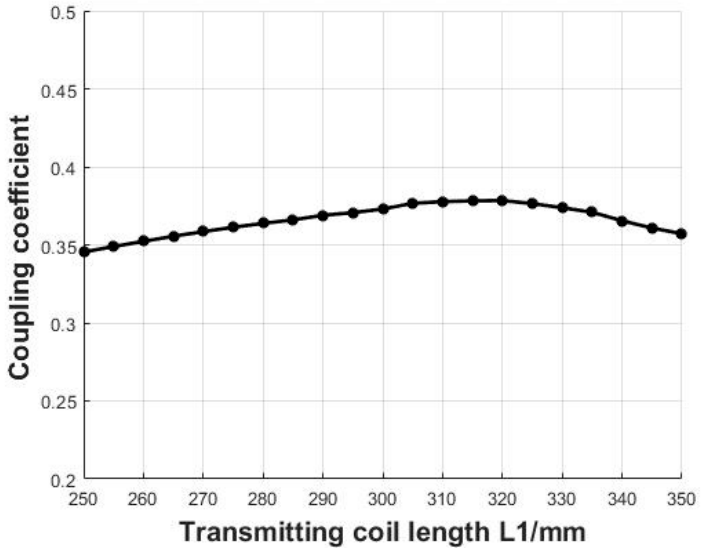

Figure 7. Simulation results of coupling coefficients at different L1.

Similarly, half the width of the core is W1, so W1 was set to vary in the range 55–100 mm, as shown in Figure 8. As W1 increases, the height of the main flux path increases, with more and more flux passing through the receiving coil. It was found that when W1 increased to 70 mm, k stopped increasing, so W1 was set to 70 mm.

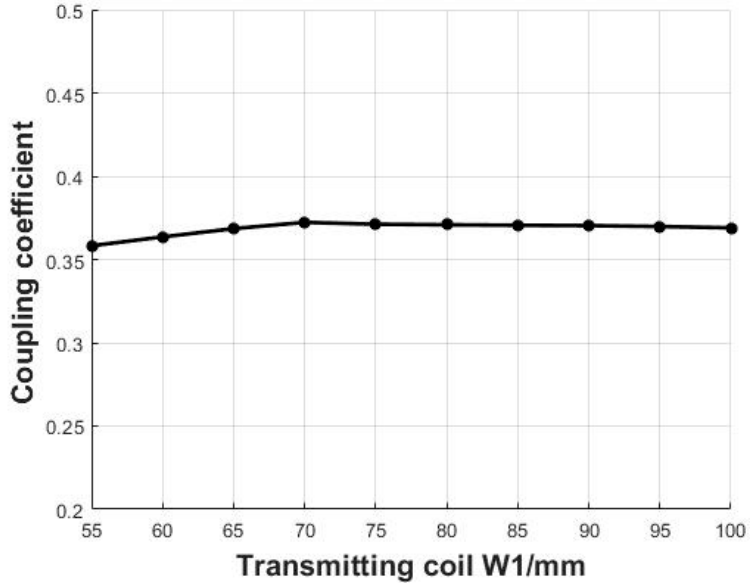

Figure 8. Simulation results of coupling coefficients for different W1.

The receiver coil height H1 varied in the range of 60–220 mm, thus H2 was determined to be 10 mm. The simulation results are shown in Figure 9, where it can be seen that the k value first increases and then decreases. Since the height of the transmitting magnetic field is limited, if the receiver coil is set too high, the leakage inductance of the receiver device will increase, but the effective flux area will not increase. To reduce the weight of the receiver, H1 was set to 150 mm.

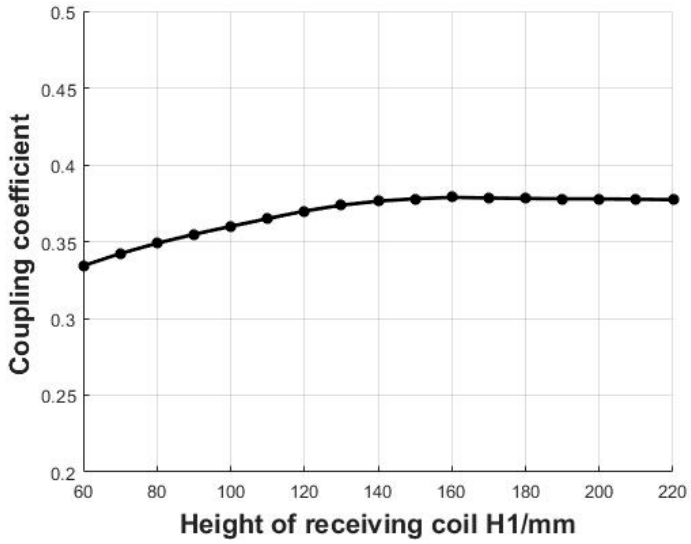

Figure 9. Simulation results of coupling coefficients at different H1.

2.3. Coupling Structure Optimization

As the UAV is disturbed by the ground's magnetic field when landing, its landing position deviates, resulting in unstable system transmission power. To improve the offset resistance of the system, the L1, W1, and H1 obtained in Section 2.2 were optimized, and L1 (290−350 mm), W1 (60−90 mm), and H1 (130−170 mm) were tested for an offset of ±90 mm in the X and Y axes within a certain range. The simulation results are shown in Figure 10.

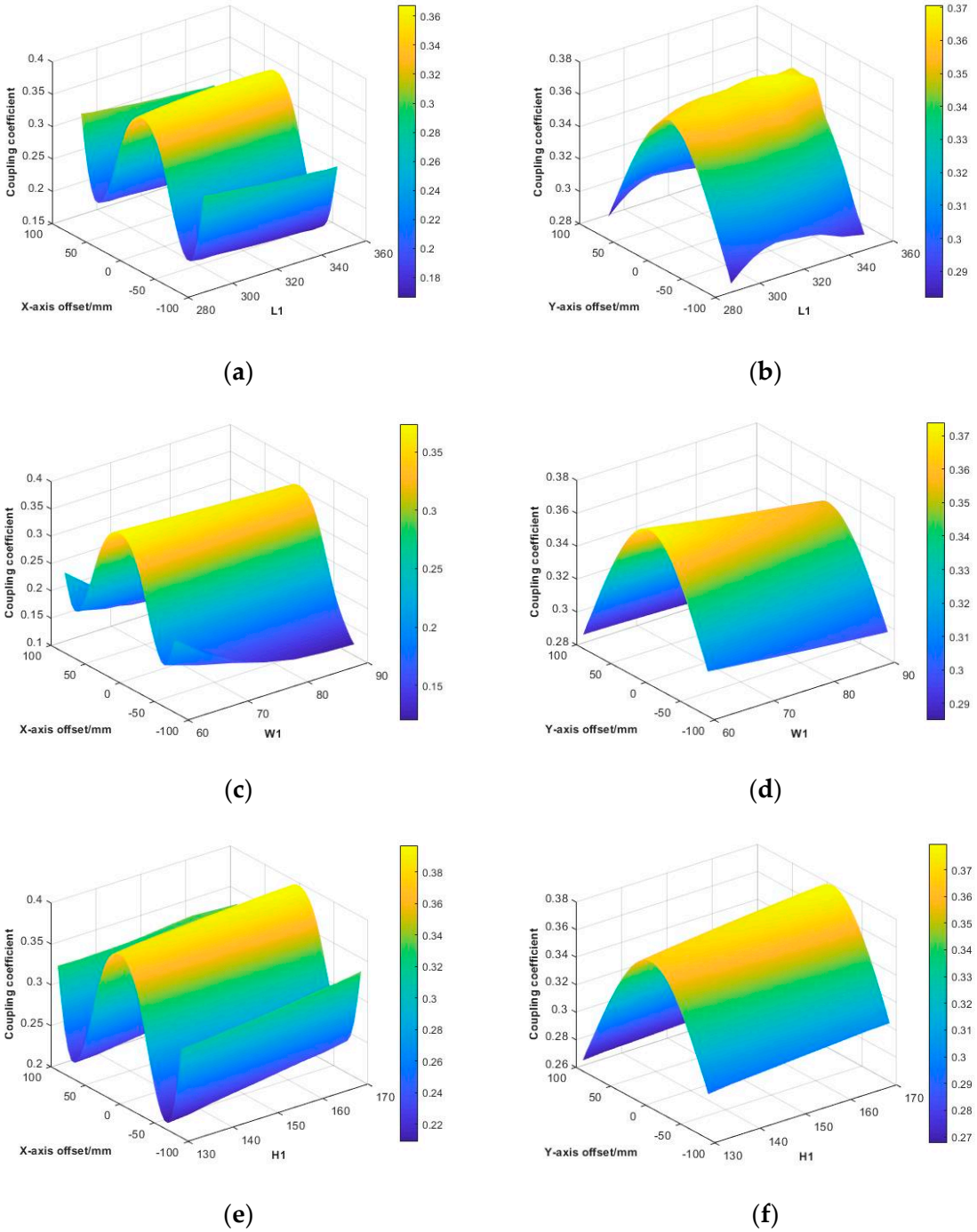

Figure 10. (**a**) Variation of coupling coefficients for different L1 lateral offsets. (**b**) Variation of coupling coefficients at different L1 longitudinal offsets. (**c**) Variation of coupling coefficients for different W1 lateral offsets. (**d**) Variation of coupling coefficients at different W1 longitudinal offsets. (**e**) Variation of coupling coefficients for different H1 lateral offsets. (**f**) Variation of coupling coefficients at different H1 longitudinal offsets.

As can be seen from Figure 10, when the system is perfectly aligned, the inter-coil coupling coefficient is larger when L1 is at 305–330 mm, about 0.368, but when the system undergoes a large offset, L1 = 305 mm shows better resistance to offset, so the value of L1 was set to 305 mm. For W1, it can be seen from the results that the coupling coefficient gradually decreases as W1 increases at system *X*-axis offset greater than 50 mm and *Y*-axis offset greater than 60 mm, while at other offset positions, the value of W1 has less influence

on the system coupling coefficient. Therefore, the value of W1 was set to 60 mm. As for the receiving coil height, H1, when the offset occurs in the *X*-axis direction, different values of H1 have less influence on the coupling capacity of the system. When the offset in the *Y*-axis is greater than 40 mm, the coupling coefficient gradually increases with the increase of H1, but the increase is not apparent. To reduce the weight of the receiving device, H1 was changed to 130 mm.

From the above analysis, the specific dimensions of the coupling structure can be derived as shown in Table 1 below:

Table 1. Coupling structure parameters.

Parameters	Values (mm)	Parameters	Values (mm)
Length of transmitting coil L1	305	Launch core length L2	240
Width of transmitting coil W4	190	Receiving coil length L3	294
Emission core width W2	120	Receiving coil height H1	130
Core width W3	28	Receiving coil width W5	3.65

2.4. Magnetic Field Distribution of the Coupling Mechanism

The flux line distribution of the designed coupling structure is shown in Figure 11a,b.

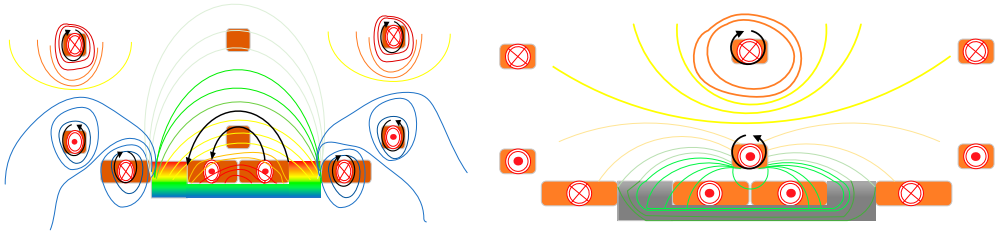

(**a**) (**b**)

Figure 11. (**a**) Distribution of magnetic flux lines in the transmitting coil (**b**) Flux line distribution in the receiving coil.

The designed concave coupled structure was simulated at the orthogonal and lateral offset positions; the resultant magnetic field distribution is shown in Figure 12. It can be seen that the concave structure has a significant suppression effect on the system leakage, and the ferrite in the structure can further direct the magnetic flux and limit the operating range of the magnetic field. The main working space for the magnetic field is within the area of 70 mm from the transmitter coil. Outside this range, the field starts to gradually then rapidly decay. The designed coupling structure ensures that the UAV body is kept out of the range of the magnetic field and ensures the safety of the UAV's internal equipment.

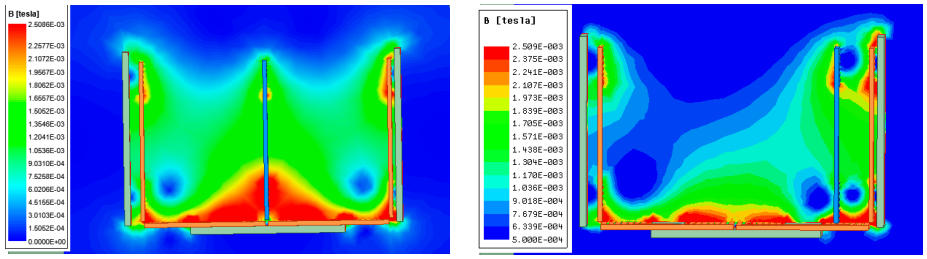

(**a**) (**b**)

Figure 12. (**a**) Magnetic field distribution during alignment of concave structures. (**b**) Magnetic field distribution during the offset of the concave structure.

2.5. Coupling Mechanism Anti−Offset Test

After the mission, the UAV can land precisely in the transmitter using GPS and visual positioning. However, a degree of misalignment may occur in particular environments and in the event of interference with sensors. In order to test the misalignment tolerance performance of the coupling structure, the optimized concave structure and presented in Section 2.2 and the conventional orthogonal structure were tested with an offset of 90−90 mm in the $X-$axis and $Y-$axis directions, respectively. The misalignment direction is shown in Figure 13, and the variation of the coupling coefficient of the system is shown in Figure 13. The results show that the orthogonal structure appears to have a reversed magnetic field when the $X-$axis is shifted, that there is some risk in the event of larger shifts, and that charging is not possible. The optimized concave structure shows a better resistance to offset, with the inter-coil coupling coefficient, k, decreasing by 49% at an offset of −70 mm on the $X-$axis and by 13.3% at an offset of 90 mm on the $Y-$axis. This coupling structure has a stronger resistance to offset in the $Y-$axis direction than in the $X-$axis direction.

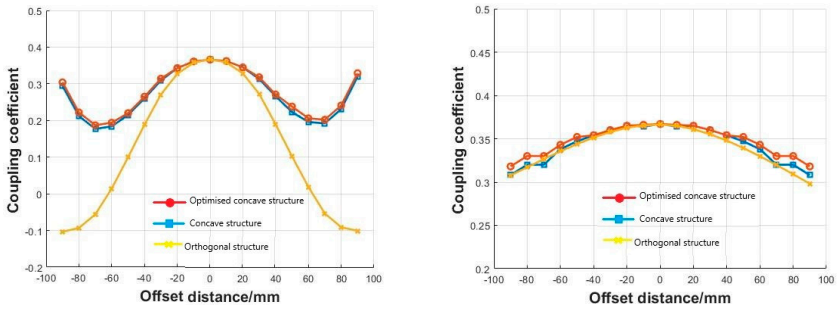

(**a**) (**b**)

Figure 13. (**a**) Variation of coupling coefficients for offset in the $X-$axis direction. (**b**) Variation of coupling coefficients for offset in the $Y-$axis direction.

For the coupling system to operate properly, a constant inductance is fundamental to the stable operation of the compensation network, so the degree of variation in the inductance of the transmitting and receiving coils of the coupling device when the system is offset also reflects the fault tolerance of the device. The variation of the inductance at the transmitting and receiving ends of the system is shown in Figure 14. The test results show that the inductance of the receiving coil varies within 2 uH, and the transmitting coil inductance varies within 0.2 uH over the offset range of −90 mm to 90 mm in both directions, with a slight change in the inductance of the coupling structure. Therefore, the coupling structure has an excellent resistance to offset.

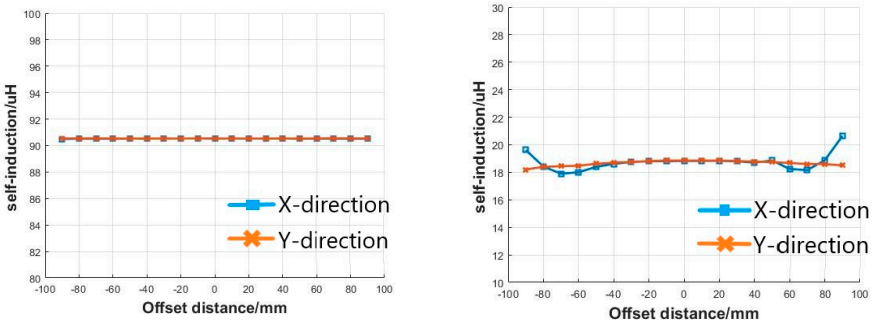

(**a**) (**b**)

Figure 14. (**a**) Variation of the original side self-inductance. (**b**) Variation of the secondary side self-inductance.

Through the above analysis, it can be seen that the designed coupling structure is small, the magnetic field working space is far away from the UAV body, and it has strong anti-offset ability, which not only ensures the transmission efficiency of the system, but also ensures the safety of the internal equipment of the UAV.

3. System Circuit and Control Design

3.1. The Double-Sided LCC Compensation Topology Analysis

The UAV wireless charging system includes an inverter circuit, a transmission coil, a compensation network, a rectifier circuit, a control unit, and a monitoring unit. The overall design of the system is shown in Figure 15. The input DC voltage is converted to 85 kHz AC through the inverter. The AC power reaches the transmitter coil through the compensation network, which excites the transmitter coil to generate the transmitting magnetic field. The receiver coil receives energy through mutual inductive coupling with the transmitter coil.

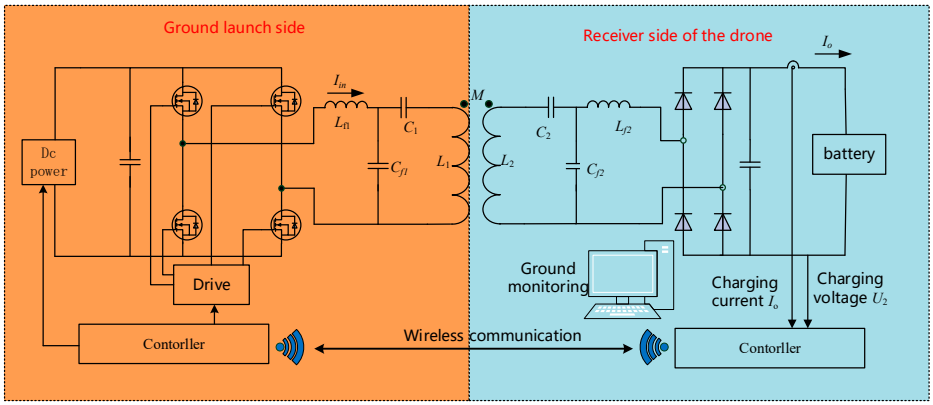

Figure 15. General block diagram of the system.

The double−sided LCC composite compensation topology was chosen for the system design. The simplified circuit model of the wireless charging system is shown in Figure 16. U_1 is the square-wave alternating current transformed by the inverter, R_L is the equivalent load of the battery and rectifier, ω is the angular frequency of the system, L_1 and L_2 are the self−inductance of the transmitting and receiving coils respectively, L_{f1} and L_{f2} are the compensation inductors, and C_{f1}, C_{f2}, C_1 and C_2 are the compensation capacitors.

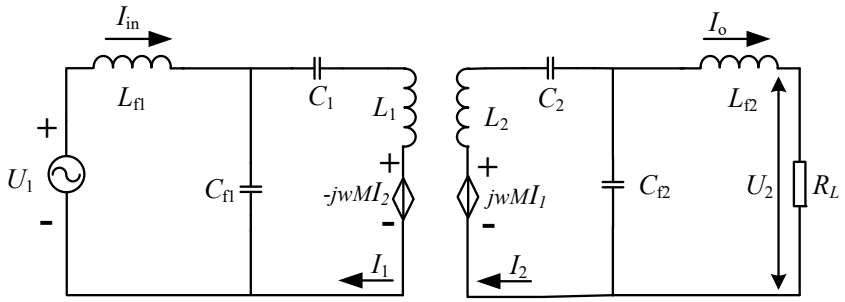

Figure 16. Simplified circuit model of the MCR-WPT system.

From the equivalent circuit model, it is possible to obtain the voltages and currents of the various parts of the system at resonance:

$$I_{in} = \frac{M^2 U_1 R_L}{\omega^2 {L_{f1}}^2 {L_{f2}}^2} = \frac{M^2 U_1 R_L}{\omega^2 {L_{f1}}^2 {L_{f2}}^2} \angle 0^\circ \tag{4}$$

$$I_1 = \frac{U_1}{j\omega L_{f1}} = \frac{U_1}{\omega L_{f1}} \angle -90^\circ \tag{5}$$

$$I_2 = \frac{MU_1R_L}{\omega^2 L_{f1}{L_{f2}}^2} = \frac{M^2U_1R_L}{\omega^2 L_{f1}{L_{f2}}^2}\angle 0^\circ \tag{6}$$

$$I_o = \frac{MU_1}{j\omega L_{f1}L_{f2}} = \frac{MU_1}{\omega L_{f1}L_{f2}}\angle -90^\circ \tag{7}$$

So the output power of the system P_o is

$$P_o = \frac{M^2{U_1}^2R_L}{\omega^2{L_{f1}}^2{L_{f2}}^2} \tag{8}$$

From Equation (7), it can be concluded that controlling the system input voltage enables the control of the output current and thus the regulation of the charging power of the battery.

3.2. Closed-loop Control System Design

In order to meet the requirement of charging Li-ion batteries with constant current followed by constant voltage, the system achieves constant current and voltage by controlling the input voltage of the inverter. The primary control flow chart of the system is shown in Figure 17. The primary controller is mainly responsible for receiving the system output information sent by the secondary side and performing closed-loop processing; the closed-loop consists of the voltage outer loop and the current inner loop. The secondary side is mainly responsible for ADC sampling in the timer, collecting the system output voltage and current information, smoothing the output processing of the data, and finally sending the data back to the ground side of the system.

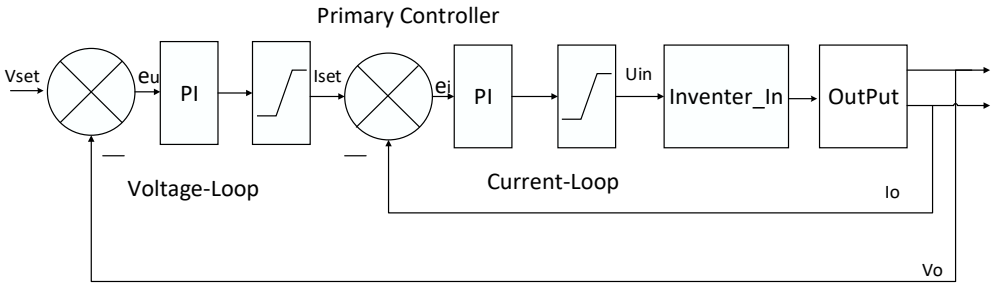

Figure 17. Flow chart of the raw edge closed loop.

When the system first starts to work, due to the low battery voltage, the voltage error is large, resulting in PI controller saturation. The system starts to charge the battery with a constant current. When the battery voltage reaches the desired voltage set by the system, through the calculation of the system voltage error is less than 0, the voltage PI controller withdraws from its saturation state, the current error is always close to 0, the current loop does not work, and the working condition of the system is constant voltage output until the end of charging.

4. System Construction and Experiment

To verify the scheme, a wireless charging test platform was built, as shown in Figure 18. The bilateral LCC topology parameters were designed with asymmetric compensation [26]. After taking Lf1/Lf2 = 1.48, Equation (7) was entered to obtain the system parameters shown in Table 2. The system operated at a fixed frequency of 85 kHz. The primary side inverter used H50ER5 SiC devices. The secondary side rectifier used a Schottky diode with a smaller voltage drop to reduce system power loss. Both the primary and secondary side controllers used DSP28335 devices. The secondary side controller was mainly responsible for the voltage and current detection of the system output state and feedback to the central controller through the wireless communication module. The primary side controller performed the closed-loop processing of the system and generated a high-

frequency inverter drive signal. The sending and receiving coils used Litz wire with a diameter of 3.65 mm, and the ferrite on the transmitting side uses manganese-zinc ferrite with better magnetic permeability.

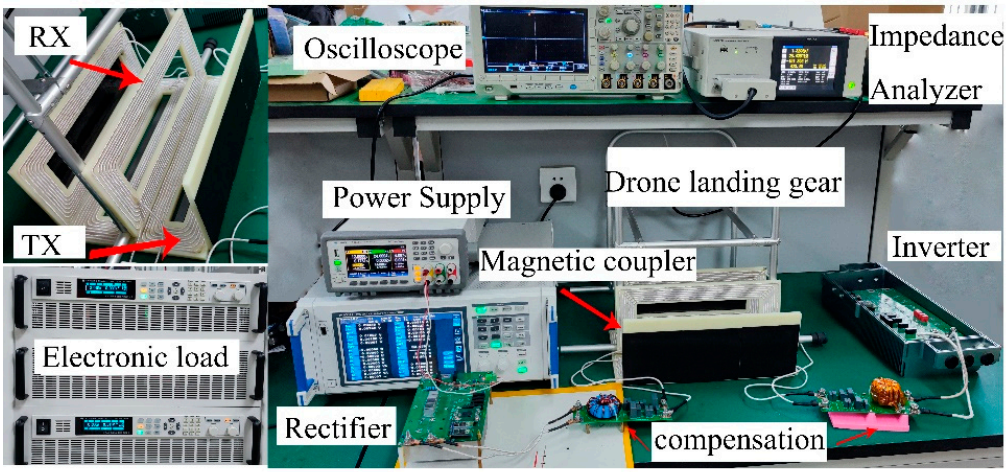

Figure 18. System experimental test platform.

Table 2. WPT system parameters.

Symbol	Value	Symbol	Value
Input voltage U_{in}	136 *V*	Primary side series capacitance C_1	45 nF
Inductance of Transmitting coil L_1	90.5 μH	Primary side shunt capacitance C_{f1}	275 nF
Inductance of receiving coil L_2	18.8 μH	Secondary side series capacitance C_2	336 nF
Primary side compensates inductance L_{f1}	12.7 μH	Secondary side shunt capacitance C_{f2}	408 nF
Auxiliary side compensates inductance L_{f2}	8.57 μH	coupling coefficient$k$	0.366
Load RL	2.4 Ω	Receiving coil weight	290 g

The power analyzer (Japan HIOKI PW6001) tested the input and output power of the system. As shown in Figure 19a, the input power of the system was 1120 W, the output power was 960 W, the overall efficiency of the system was 85.7%, the charging voltage was 48 V, and the charging current was 20 A, which meets the design requirements of the system. The conversion efficiency of the inverter was 96%, The output waveform of the inverter measured by the oscilloscope (USA Tektronix MDO3014) is shown in Figure 19c; the transmission efficiency of the coupling structure was 94%, the efficiency of the rectifier was 95%, and the remaining losses were mainly reflected in the loss of the conduction line. The rectifier uses uncontrollable rectification, and if it is replaced by controllable rectification, the efficiency can be further improved.

The system's output was connected to the electronic load of the Dahua (China DH27603B) power supply to simulate the state of charging the battery, so the first stage of the system state was 20 A constant current charging, and the second stage was 48 V regular voltage charging. In the constant current phase, the charging voltage may vary in the range of 30–50 V, corresponding to an equivalent load value of 1.5–2.5 Ω. The system's output voltage in the constant voltage phase was 48 V, and the output current varied from 1–20 A until the end of charging, corresponding to an equivalent load variation of 2.4–48 Ω. Figure 20 shows how the output voltage varied with the equivalent load during the constant current phase and how the current varied with the equivalent load during the constant voltage phase. The results show that the output voltage and current of the system are consistent with the set values and that the system can achieve closed-loop charging with constant current/voltage.

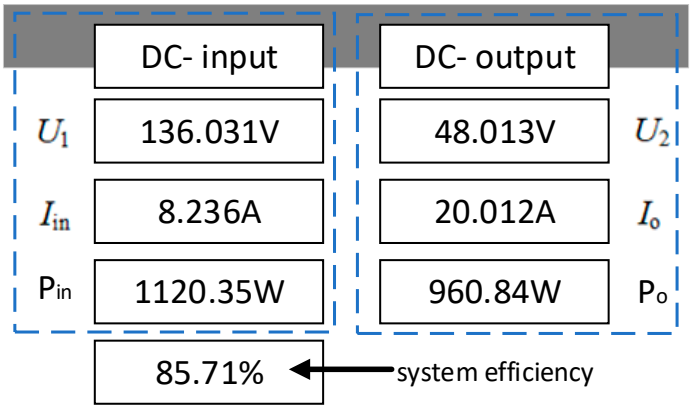

(**a**)

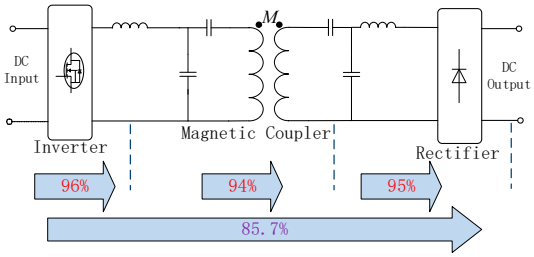

(**b**)

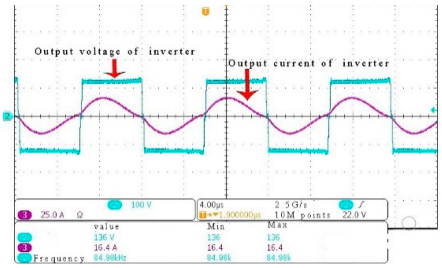

(**c**)

Figure 19. Rated power test for the 2.4 Ω fixed resistive load. (**a**) DC-input and charging output power. (**b**) System Loss Analysis. (**c**) Inverter working waveform.

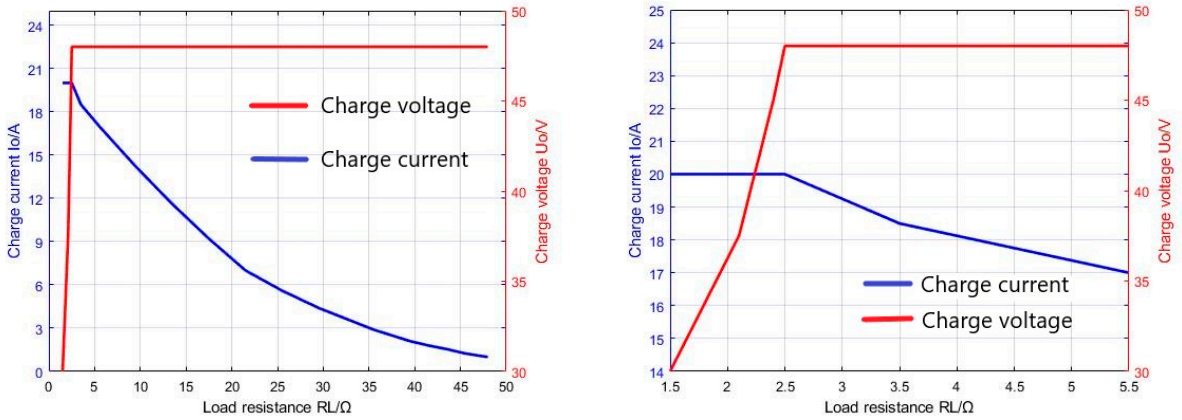

(**a**) (**b**)

Figure 20. Charging voltage and current versus load resistance. (**a**) Change the load resistance from 1.5 Ω to 48 Ω. (**b**) Change the load resistance from 1.5 Ω to 5.5 Ω.

To test the resistance to offset, the variation of the output current and efficiency of the system in the $X-$and $Y-$axes for an open$-$loop test system at an equivalent load of 2.4 Ω was measured; the results are shown in Figure 21. The results show that at an equivalent load of 2.4 Ω, the charging current was above 9.7 A when the system was offset in the $X-$and $Y-$axis directions [−90 mm, 90 mm] as a whole, and the efficiency of the whole machine was not less than 79%, which ensures the regular operation of the system.

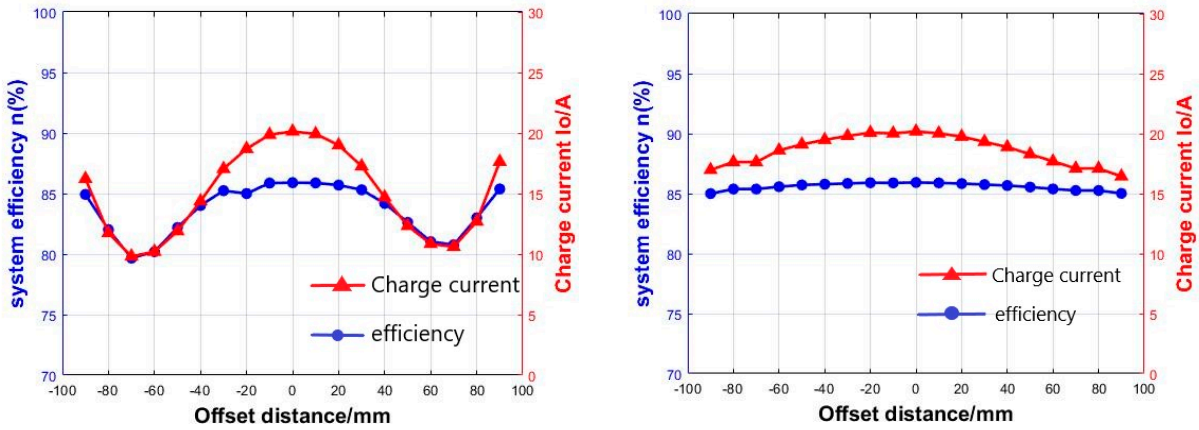

Figure 21. Charging power and system efficiency versus (**a**) lateral displacement and (**b**) longitudinal displacement.

5. Discussion

The design proposed in this paper shows good resistance to offset in both the *X*- and *Y*-axes, and the small size and light weight of the receiver reduces the workload on the UAV, which potentially expands the unmanned working range of drones. In the future, the application of UAVs in the unattended sector will become more and more widespread, and the environments in which UAVs are charged wirelessly will become more complex, There may be metal or other foreign objects between the coupling structures, and this design has not been thoroughly studied in terms of foreign object detection. Therefore, the question of how to adapt to changing environments will become the focus of future research.

6. Conclusions

This paper focused on a concave coupling structure for the wireless charging of UAVs. For this purpose, transmitting and receiving coils with strong anti-offset capability were designed. The proposed receiver end is light in weight, reducing the workload of the UAV and solving the problems of complex installation and the large size of the receiver end. Experimental results showed that the wireless charging system can effectively charge at 48 V and 20 A with a charging efficiency of up to 85.7%. In the future, GaN devices with smaller switching loss and higher frequency will be used to further improve the system efficiency, and the transmission system that can adapt to various complex environments will be designed to expand the application range of the coupling structure.

Author Contributions: Conceptualization, L.Y. and L.W.; methodology, Y.Z.; software, L.Y.; validation, L.Y., G.Z. and S.X.; formal analysis, X.C.; investigation, L.Y.; resources, Y.Z.; data curation, L.Y.; writing—original draft preparation, L.Y.; writing—review and editing, L.W.; visualization, L.Y. and G.Z.; supervision, Y.Z.; project administration, X.C.; funding acquisition, Y.Z. All authors have read and agreed to the published version of the manuscript.

Funding: This research was funded by key R&D project of Sichuan Province (21ZDYF3793).

Data Availability Statement: Data is available on request. The corresponding author Langtao Yu can be contacted to request the data. To request the data, please contact swust_ylt@163.com.

Acknowledgments: This paper was funded by key R&D project of Sichuan Province, grant number 21ZDYF3793.

Conflicts of Interest: The funders had no role in the design of the study; in the collection, analyses, or interpretation of data; in the writing of the manuscript, or in the decision to publish the results.

References

1. Long, T.; Ozger, M.; Cetinkaya, O.; Akan, O.B. Energy Neutral Internet of Drones. *IEEE Commun. Mag.* **2018**, *56*, 22–28. [CrossRef]
2. Li, Z.; Mu, S.; Li, J.; Wang, W.; Liu, Y. Transmission line intelligent inspection central control and mass data processing system and application based on UAV. In Proceedings of the 4th International Conference on Applied Robotics for the Power Industry, Jinan, China, 11–13 October 2016; pp. 1–5.
3. Zhang, Z.; Pang, H.; Georgiadis, A.; Cecati, C. Wireless Power Transfer -An Overview. *IEEE Trans. Ind. Electron.* **2019**, *66*, 1044–1058. [CrossRef]
4. Richardson, P.L. Upwind dynamic soaring of albatrosses and UAVs—ScienceDirect. *Prog. Oceanogr.* **2015**, *130*, 146–156. [CrossRef]
5. Oettershagen, P.; Melzer, A.; Mantel, T.; Rudin, K.; Lotz, R.; Siebenmann, D.; Leutenegger, S.; Alexis, K.; Siegwart, R. A solar-powered hand-launchable UAV for low-altitude multi-day continuous flight. In Proceedings of the IEEE International Conference on Robotics & Automation, Seattle, WA, USA, 26–30 May 2015; IEEE: Piscataway, NJ, USA, 2015; pp. 3986–3993.
6. Tavakoli, R.; Pantic, Z. Analysis, Design and Demonstration of a 25-kW Dynamic Wireless Charging System for Roadway Electric Vehicles. *IEEE J. Emerg. Sel. Top. Power Electron.* **2017**, *6*, 1378–1393. [CrossRef]
7. Jayalath, S.; Khan, M.A. Design, Challenges, and Trends of Inductive Power Transfer Couplers for Electric Vehicles: A Review. *IEEE J. Emerg. Sel. Top. Power Electron.* **2020**, *9*, 6196–6218. [CrossRef]
8. Sampath, J.P.K.; Alphones, A.; Shimasaki, H. Coil design guidelines for high efficiency of wireless power transfer (WPT). In Proceedings of the 2016 IEEE Region 10 Conference (TENCON), Singapore, 22–25 November 2016; pp. 726–729.
9. Jolani, F.; Yu, Y.; Chen, Z. A novel planar wireless power transfer system with strong coupled magnetic resonances. In Proceedings of the 2014 IEEE International Wireless Symposium (IWS 2014), Xi'an, China, 24–26 March 2014.
10. Kumar, S.; Jayprakash, G.K.M. Wireless power transfer for the unmanned aerial vehicle (UAV) charging. *Int. Res. J. Eng. Technol.* **2017**, *4*, 1939–1942.
11. Song, Y.; Sun, X.; Wang, H.; Dong, W.; Ji, Y. Design of Charging Coil for Unmanned Aerial Vehicle-Enabled Wireless Power Transfer. In Proceedings of the 2018 8th International Conference on Power and Energy Systems (ICPES), Colombo, Sri Lanka, 21–22 December 2018; IEEE: Piscataway, NJ, USA, 2018.
12. Campi, T.; Dionisi, F.; Cruciani, S.; De Santis, V.; Feliziani, M.; Maradei, F. Magnetic field levels in drones equipped with Wireless Power Transfer technology. In Proceedings of the Asia-Pacific International Symposium on Electromagnetic Compatibility, Shenzhen, China, 17–21 May 2016; IEEE: Piscataway, NJ, USA, 2016.
13. Abatti, P.J.; de Miranda, C.M.; da Silva, M.A.; Pichorim, S.F. Analysis and optimisation of three-coil wireless power transfer systems. *IET Power Electron.* **2018**, *11*, 68–72. [CrossRef]
14. Li, Y.; Xu, Q.; Lin, T.; Hu, J.; He, Z.; Mai, R. Analysis and Design of Load-Independent Output Current or Output Voltage of a Three-Coil Wireless Power Transfer System. *IEEE Trans. Transp. Electrif.* **2018**, *4*, 364–375. [CrossRef]
15. Cai, C.; Wang, J.; Nie, H.; Zhang, P.; Lin, Z.; Zhou, Y.G. Effective-Configuration WPT Systems for Drones Charging Area Extension Featuring Quasi-Uniform Magnetic Coupling. *IEEE Trans. Transp. Electrif.* **2020**, *6*, 920–934. [CrossRef]
16. Jeong, S.; Bito, J.; Tentzeris, M.M. Design of a novel wireless power system using machine learning techniques for drone applications. In Proceedings of the 2017 IEEE Wireless Power Transfer Conference (WPTC), Taipei, Taiwan, 10–12 May 2017; IEEE: Piscataway, NJ, USA, 2017.
17. Li, J.; Yin, F.; Wang, L.; Cui, B.; Yang, D. Electromagnetic Induction Position Sensor Applied to Anti-Misalignment Wireless Charging for UAVs. *IEEE Sens. J.* **2019**, *20*, 515–524. [CrossRef]
18. Han, W.; Chau, K.T.; Jiang, C.; Liu, W.; Lam, W.H. Design and Analysis of Quasi-Omnidirectional Dynamic Wireless Power Transfer for Fly-and-Charge. *IEEE Trans. Magn.* **2019**, *55*, 8001709. [CrossRef]
19. Wang, S.; Hu, Z.; Rong, C.; Lu, C.; Chen, J.; Liu, M. Planar Multiple-Antiparallel Square Transmitter for Position-Insensitive Wireless Power Transfer. *IEEE Antennas Wirel. Propag. Lett.* **2018**, *17*, 188–192. [CrossRef]
20. Wu, S.; Cai, C.; Jiang, L.; Li, J.; Yang, S. Unmanned Aerial Vehicle Wireless Charging System With Orthogonal Magnetic Structure and Position Correction Aid Device. *IEEE Trans. Power Electron.* **2020**, *36*, 7564–7575. [CrossRef]
21. Song, C.; Kim, H.; Kim, Y.; Kim, D.; Jeong, S.; Cho, Y.; Lee, S.; Ahn, S.; Kim, J. EMI Reduction Methods in Wireless Power Transfer System for Drone Electrical Charger Using Tightly Coupled Three-Phase Resonant Magnetic Field. *IEEE Trans. Ind. Electronics* **2018**, *65*, 6839–6849. [CrossRef]
22. Campi, T.; Cruciani, S.; Feliziani, M.; Maradei, F. High efficiency and lightweight wireless charging system for drone batteries. In Proceedings of the AEIT International Conference, Cagliari, Italy, 20–22 September 2017; pp. 1–6.
23. Junaid, A.B.; Konoiko, A.; Zweiri, Y.; Sahinkaya, M.N.; Seneviratne, L. Autonomous Wireless Self-Charging for Multi-Rotor Unmanned Aerial Vehicles. *Energies* **2017**, *10*, 803. [CrossRef]

24. Chae, H.; Park, J.; Song, H.; Kim, Y.; Jeong, H. The IoT based automate landing system of a drone for the round-the-clock surveillance solution. In Proceedings of the IEEE International Conference on Advanced Intelligent Mechatronics, Busan, Korea, 7–11 July 2015; IEEE: Piscataway, NJ, USA, 2015.
25. Zhu, Y.; Wang, Z.; Cao, X.; Wu, L. Design of High-Power High-Efficiency Wireless Charging Coils for EVs with MnZn Ferrite Bricks. *J. Sens.* **2021**, *2021*, 9931144. [CrossRef]
26. Chen, Y.; Zhang, H.; Shin, C.S.; Jo, C.H.; Park, S.J.; Kim, D.H. An Efficiency Optimization-Based Asymmetric Tuning Method of Double-Sided LCC Compensated WPT System for Electric Vehicles. *IEEE Trans. Power Electron.* **2020**, *35*, 11475–11487. [CrossRef]